Prostate implant reconstruction from C-arm images with motion-compensated tomosynthesis

Ehsan Dehghan
School of Computing, Queen's University, Kingston, Ontario K7L-3N6, Canada

Mehdi Moradi, Xu Wen, Danny French, and Julio Lobo
Department of Electrical and Computer Engineering, University of British Columbia, Vancouver, British Columbia V6T-1Z4, Canada

W. James Morris
Vancouver Cancer Centre, Vancouver, British Columbia V5Z-1E6, Canada

Septimiu E. Salcudean[a)]
Department of Electrical and Computer Engineering, University of British Columbia, Vancouver, British Columbia V6T-1Z4, Canada

Gabor Fichtinger
School of Computing, Queen's University, Kingston, Ontario K7L-3N6, Canada

(Received 15 May 2011; revised 12 July 2011; accepted for publication 8 August 2011; published 9 September 2011)

Purpose: Accurate localization of prostate implants from several C-arm images is necessary for ultrasound-fluoroscopy fusion and intraoperative dosimetry. The authors propose a computational motion compensation method for tomosynthesis-based reconstruction that enables 3D localization of prostate implants from C-arm images despite C-arm oscillation and sagging.
Methods: Five C-arm images are captured by rotating the C-arm around its primary axis, while measuring its rotation angle using a protractor or the C-arm joint encoder. The C-arm images are processed to obtain binary seed-only images from which a volume of interest is reconstructed. The motion compensation algorithm, iteratively, compensates for 2D translational motion of the C-arm by maximizing the number of voxels that project on a seed projection in all of the images. This obviates the need for C-arm full pose tracking traditionally implemented using radio-opaque fiducials or external trackers. The proposed reconstruction method is tested in simulations, in a phantom study and on ten patient data sets.
Results: In a phantom implanted with 136 dummy seeds, the seed detection rate was 100% with a localization error of 0.86 ± 0.44 mm (Mean $\pm$ STD) compared to CT. For patient data sets, a detection rate of 99.5% was achieved in approximately 1 min per patient. The reconstruction results for patient data sets were compared against an available matching-based reconstruction method and showed relative localization difference of 0.5 ± 0.4 mm.
Conclusions: The motion compensation method can successfully compensate for large C-arm motion without using radio-opaque fiducial or external trackers. Considering the efficacy of the algorithm, its successful reconstruction rate and low computational burden, the algorithm is feasible for clinical use. [DOI: 10.1118/1.3633897]

Key words: tomosynthesis, brachytherapy, seed reconstruction, motion compensation, C-arm

I. INTRODUCTION

Since its advent in the early 1980s, ultrasound-guided prostate brachytherapy (hereafter brachytherapy) has become a definitive treatment option for prostate cancer—the leading cancer among men in the United States in 2010 (Ref. 1)—with outcomes comparable to the radical prostatectomy that is considered as the gold standard.[2–4] The goal of brachytherapy is to kill the cancer in the prostate gland with radiation by permanently implanted radioactive ^{125}I or ^{103}Pd capsules (seeds). Seed positions are carefully planned to deliver a lethal radioactive dose to the cancerous prostate, while maintaining a tolerable dose to the urethra and rectum. The brachytherapist delivers the seeds using needles under visual guidance from transrectal ultrasound (TRUS) and qualitative assessment from frequently acquired fluoroscopy images.[5]

The success of brachytherapy depends on accurate placement of the seeds. However, prostate motion and deformation,[6] needle bending, prostate swelling,[7] seed migration,[8] and human and system calibration errors can result in seed misplacement which, in turn, can lead to underdosed regions or over-radiation of the surrounding healthy tissue. In current brachytherapy practice, the implant is quantitatively assessed using CT, postoperatively. In case of major underdosing, external beam radiation is applied as an adjunct. Intraoperative dosimetry can provide the physicians with quantitative

dose assessment in the operating room and enable them to adjust the position and number of the remaining seeds to compensate for the developing cold spots.[9–11]

Three dimensional localization of the implanted seeds, registered to the prostate anatomy, is required for dose calculation. TRUS provides sufficient soft tissue contrast to delineate the prostate boundaries. However, despite significant efforts in seed localization from ultrasound,[12–18] robust seed segmentation in ultrasound is not yet possible. It was shown that up to 25% of the seeds can be missed even through manual segmentation of B-mode images.[12]

Mobile C-arms are routinely used in the contemporary prostate brachytherapy for implant visualization. However, the prostate cannot be visualized in the C-arm images. Therefore, TRUS-fluoroscopy fusion offers itself as a practical solution for intraoperative dosimetry.[10,19–22] In these methods, the seeds reconstructed from C-arm images are spatially registered to the prostate volume visible in TRUS images. The delivered dose to the prostate is evaluated and the plan is modified, accordingly.

The reconstruction of the implanted seeds in 3D space from several x-ray images has been widely studied.[23–38] These efforts can be categorized into two major groups. In the first group, 2D coordinates of the seed projection centers are identified in the images and a matching problem is solved to identify the corresponding projections of each seed in different images.[23,25–32] These methods should be preceded with a complicated seed segmentation method to precisely localize the seed projection centroids.[39–41] It is difficult, or sometimes impossible, to localize the centroid of each individual seed projection in an image due to presence of hidden and overlapping seed projections (see Fig. 1). Therefore, manual intervention is usually necessary in the seed segmentation phase. However, even after manual intervention, some seed projections can remain hidden. Although some seed matching algorithms can address the hidden seed problem,[27–29,31,32] the performance of these algorithms usually degrades with increasing number of hidden seeds.

The second group of seed reconstruction methods consists of tomosynthesis-based algorithms.[24,33–37] The tomosynthesis-based reconstruction methods have two advantages over the seed matching methods. First, the matching problem in the presence of hidden or overlapping seed projections is inherently solved by tomosynthesis. Therefore, these methods do not need a seed matching algorithm. Second, the tomosynthesis-based reconstruction methods require a much simpler seed segmentation algorithm, as they do not rely on localization of seed projection centroids in every image. A binary image that only separates the seed projections from the background—without localization of their centers—suffices for a tomosynthesis-based seed reconstruction.

Tomosynthesis-based seed reconstruction is especially attractive for reconstruction of ^{125}I seeds, which have a larger projection compared to ^{103}Pd seeds. Due to their relatively larger seed projections, overlapping and hidden seed projections are more abundant in the C-arm images of ^{125}I implants. Therefore, seed segmentation for matching-based reconstruction is considerably more difficult for ^{125}I seeds.

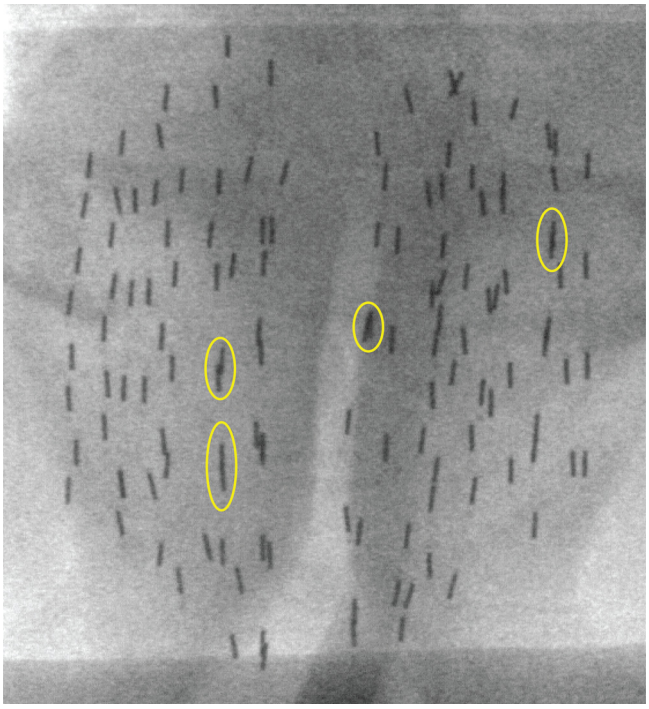

FIG. 1. A typical C-arm image of an implant showing some of the overlapping and hidden seeds. Localization of the seed projection centroids for hidden or overlapping seeds is difficult or sometimes impossible for seed segmentation methods.

This makes tomosynthesis, the preferred method for ^{125}I seed reconstruction. However, it should be noted that tomosynthesis-based reconstructions can be used to reconstruct ^{103}Pd seeds without any restrictions.

Pokhrel *et al.*[38] introduced a seed reconstruction method based on forward projection using cone-beam CT (CBCT). Similarly to tomosynthesis-based methods, their algorithm does not rely on identification of seed projection centroids. However, their method is computationally more extensive compared to tomosynthesis-based algorithms. Also, importantly, CBCT requires a high-end digitally encoded C-arm that is typically not available in brachytherapy. In addition, CBCT demands many C-arm images, exposing the patient and OR crew to more toxic radiation.

C-arm pose—the relative positions of images in 3D space—must be known prior to seed reconstruction. Although, external electromagnetic or optical trackers can yield the C-arm pose,[42] they are not practically viable due to their cost and added complexity. The C-arm pose can be also computed using radio-opaque fiducials.[24,43–47] However, fiducials require segmentation,[41] may overlap with the anatomy of interest, occupy precious real estate in the image, and are not part of the standard operating room.

C-arm images are generally acquired by rotating the C-arm around the patient. In ideal cases, C-arm rotation angles can yield accurate pose. However, in real cases, unmeasured C-arm translational motions caused by oscillation and sagging lead to errors in the pose computation and in turn, failure of seed reconstruction.

Researchers have developed approaches to reconstruct the seeds and use them to improve the pose computation, iteratively.[25,48,49] In these methods, the seeds are reconstructed in 3D using an initial estimate of the pose. Then, a motion compensation method uses the reconstructed seeds to compensate for the errors in pose computation. In Ref. 49, we compensated for 2D translational motion of the C-arm using the reconstructed seeds, in a matching-based reconstruction scheme. The initial pose was obtained from measurements of C-arm rotation angles without external trackers or fiducials.

The aforementioned motion compensation methods, including our own work,[49] were all developed for matching-based seed reconstruction and hence, cannot be applied to a tomosynthesis-based reconstruction method. Lee *et al.*[37] were the first to use a motion compensation method within a tomosynthesis-based reconstruction. They used a radio-opaque tracking fiducial [called FTRAC Ref. (46)] to initially estimate the pose of a C-arm. At the beginning, three images with the best corresponding pose computation quality—based on the residual error of the pose recovery using FTRAC—were used to reconstruct some candidate seeds. Then, the reconstructed candidate seeds were used to improve on the pose and calibration parameters for the remaining images in a process they called "autofocus." Finally, the seeds were reconstructed using all the images. If FTRAC is not used, the quality of the initial pose computation is not known. Therefore, the three images with the best pose cannot be selected to initialize the reconstruction. In addition, without FTRAC, a tomosynthesis-based seed reconstruction may fail to reconstruct an adequate number of candidate seeds for pose correction, since initial pose computation may not be sufficiently accurate.

In this paper, we introduce a new computational motion compensation algorithm for tomosynthesis-based seed reconstruction. This method compensates for the C-arm motion by maximizing the number of seed voxels in a volume of interest. In contrast to the previous work, this method does not rely on reconstructed seeds to compensate for C-arm motion. Therefore, it can be used to compensate for large motions that prohibit initial reconstruction of a sufficient number of seeds for seed-based motion compensation. The proposed motion compensation method is especially targeted for tomosynthesis-based reconstruction. Therefore, our method inherits the advantages of a tomosynthesis-based reconstruction—such as requiring a simple segmentation and inherently solving the hidden seeds problem—which make it the preferred choice for reconstruction of ^{125}I seeds. However, this method is not limited to reconstruction of ^{125}I seeds and can be used to reconstruct ^{103}Pd seeds as well.

Similarly to Ref. 49, we initialize the pose by sole measurement of C-arm rotation angles. On the one hand, this obviates the need for full pose tracking using radio-opaque fiducials or external trackers. But, on the other hand, this initial pose estimation can fail to provide us with an adequate number of seeds for seed-based pose correction through tomosynthesis. As we will show in Sec. III, maximizing the number of seed voxels in a volume of interest, without explicit reconstruction of any seeds, surmounts this obstacle and yields accurate C-arm pose computations for successful seed reconstruction.

In Ref. 49, we demonstrated that by making realistic and practical assumptions in defining the imaging protocol in accordance with clinical limitations, a 2D motion compensation scheme will result in a clinically acceptable seed reconstruction. In this paper, we build our motion compensation on the same assumptions.

We assume that:

1. The images are taken by rotating the C-arm around its primary axis PA (y_w axis in Fig. 2) in a limited angle span, while the angle around the secondary axis (SA) is fixed (see Fig. 2).
2. C-arm rotation angles are measured.
3. The intrinsic parameters of the C-arm, such as source to image distance, source to center of rotation distance, image center and image resolution are known and do not change during the C-arm rotation.
4. Significant C-arm motions are translational motions in the Oy_wz_w plane and motion along x_w is negligible.

Single-axis rotation of the C-arm around its PA is common practice in contemporary brachytherapy. Usually, the PA is approximately aligned with the patient's craniocaudal axis. C-arm rotation angles can be measured using the device joint encoders (if available), digital protractors or accelerometers.[50] Our results in Sec. III C suggest that an accuracy of $\pm 1^\circ$, which is provided by C-arm joint encoders, is sufficient for successful reconstructions. The intrinsic parameters of the C-arm can be measured preoperatively. Since the span of C-arm rotation in a clinical setting is generally restricted to $\pm 10^\circ$ due to space limitations, the intrinsic parameters do not significantly change. Jain *et al.*[51] showed that recalibration is unnecessary since small changes in the calibration

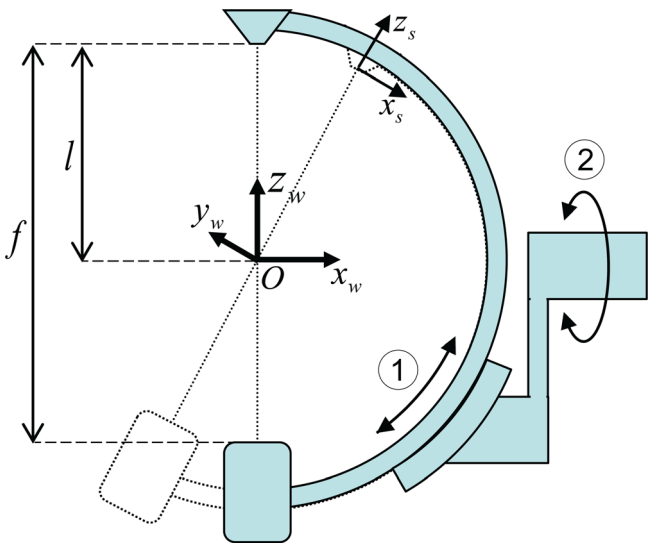

FIG. 2. Schematic of a C-arm rotating around its PA (rotation ①). Rotation ② shows rotation of the C-arm around its SA. The homogeneous world coordinate system $Ox_wy_wz_w$ is centered at the center of rotation. The homogeneous source coordinate system $Ox_sy_sz_s$ is centered at the source position corresponding to each image.

parameters do not have a significant effect on the relative position of the reconstructed seeds. Note that we are interested in the relative position of the seeds, since the reconstructed seeds will be registered to the prostate anatomy for dosimetry.[22]

The C-arm forms a cantilever at its connection to the body of the device. The intensifier is heavy and its weight creates a significant torque around the connection point that can lead to significant sagging along the z axis. In addition, due to the length of the C-arm, forces along the y and z axes can create significant torques around this joint (connection to the body) and can cause oscillation in the C-arm. However, the forces along the x axis cannot produce significant torque around this joint. Therefore, the motion caused by the forces along the x axis can only result in translation of the whole C-arm and its body along the x axis. Due to the heavy weight of the C-arm, small forces along this axis cannot cause significant motion when the C-arm wheels are locked.

Assume that images $I_i, i \in \{1,\ldots,M\}$ were acquired from a set of seeds located at $s_j = [s_{jx}, s_{jy}, s_{jz}]^T$, $j \in \{1,\ldots,N\}$, while the C-arm source positions were located at $q_i = [q_{ix}, q_{iy}, q_{iz}]^T, i \in \{1,\ldots,M\}$, where $(.)^T$ denotes the transpose of a vector or a matrix. It can be shown that, using the same set of images I_i with the same rotation angles, any C-arm source position configuration $q'_i = [q'_{ix}, q'_{iy}, q'_{iz}]^T$, $i \in \{1,\ldots,M\}$ that satisfies $(q'_i - q_1) = \lambda(q_i - q_1)$ will result in a set of reconstructed seeds (s'_i) in which, $(s'_i - q_1) = \lambda(s_i - q_1)$. In other words, a 3D translational motion compensation can result in a reconstruction with an arbitrary scale (λ). If a fiducial is used, a known length on the fiducial can be used to recover the scale.[48] In order to avoid the scaling problem without a fiducial, we take advantage of the confined motion of the C-arm and assume that the C-arm motion along x_w is negligible. Therefore, we assume that our initial C-arm pose estimations are accurate along the x_w axis (q_{ix}) and we add the constraint $(q'_{ix} - q_{1x}) = (q_{ix} - q_{1x})$ to our equations.

Our assumption about 2D motion of a C-arm is an approximation to the C-arm motion pattern. However, we show in Sec. III, that this approximation is sufficiently accurate for successful reconstruction of brachytherapy implants and results in a negligible error in the estimation of the scale (Table II).

In Sec. II, the methods for tomosynthesis-based seed reconstruction and motion compensation are outlined. Section III shows our numerical simulation, phantom, and clinical results. We discuss our results in Sec. IV, followed by conclusions and future work in Sec. V.

II. MATERIAL AND METHODS

II.A. Image processing and labeling

We use seed-only C-arm images to reconstruct the seeds. A seed-only image is a binary image in which each pixel has a value of 1, if it belongs to a seed projection and zero otherwise. An example of such an image is shown in the left side of Fig. 3. Note that in contrast to seed segmentation for matching-based reconstruction methods, we do not require the seed projection centroids to be localized. We relied on local thresholding and morphological filtering to produce the seed-only images as explained in Refs. 19 and 52. There are several other methods that can be used to produce the seed-only images.[18,34,36,39–41] Therefore, we do not discuss image processing in more details in this paper. It should be noted that a false positive projection does not result in a false positive seed, unless there are corresponding false positives in all the other images, and this is very unlikely to occur. However, a missing seed projection in one image, results in a missing seed in the reconstructed seed cloud. Therefore, manual identification of missing seed projections is necessary; however, removal of false positives is precautionary.

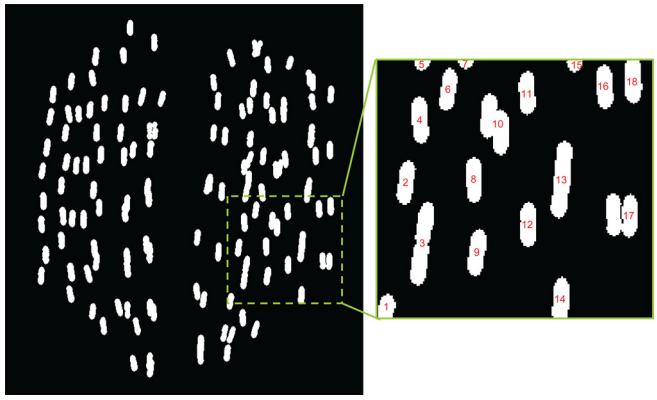

FIG. 3. Left: a dilated seed-only image, right: labeled seed-only image.

In order to increase the likelihood of seed detection and compensate for small pose computation errors, the seed-only images are dilated with a disk structural element of radius r (2–3 pixels in this work).

The dilated seed-only images are then labeled using the connected component labeling algorithm.[53] These labeled images are later used to detect and remove false positives.[35,37] More details are discussed in Sec. II D. A portion of a labeled image is shown in Fig. 3. Note that one or more seed projections can be associated with one label.

II.B. Volume of interest reconstruction

Figure 2 shows the geometry of a C-arm rotated around its primary axis (PA). Every point s in the world homogeneous coordinate system—centered at $Ox_wy_wz_w$—can be projected on a point p on the ith segmented image homogeneous coordinate system using the following equation:

$$\underline{p} = \begin{bmatrix} -f/\rho_x & 0 & c_x & 0 \\ 0 & -f/\rho_y & c_y & 0 \\ 0 & 0 & 1 & 0 \end{bmatrix} {}^s\mathbf{T}^i_w \underline{s} = \mathbf{P}_i \underline{s}, \quad (1)$$

where ${}^s\mathbf{T}^i_w$ is the transformation matrix from the world homogeneous coordinate system to the source homogeneous coordinate system centered at the x-ray source location that corresponds to the ith image, f is the source to image distance, ρ_x and ρ_y are pixel spacings along the horizontal and vertical axes of the image, c_x and c_y are the coordinates of the image center and $\underline{s}$ represents the coordinates of s in the world homogeneous coordinate system. $\mathbf{P}_i$ is a 3×4

projection matrix from the world homogeneous coordinate system to the image i homogeneous coordinate system. The point p has a pixel value $\psi_i(\underline{p})$ equal to 1, if p is inside a seed projection and equal to 0, otherwise.

We assume a volume of interest (VOI) in the 3D space. For every voxel v in the VOI with coordinates $\underline{v}$ in the world coordinate system, the voxel value is defined as:

$$\Psi(\underline{v}) = \sum_{i=1}^{M} \psi_i(\mathbf{P}_i \underline{v}), \tag{2}$$

where M is the number of images. A voxel is assumed to belong to a seed cluster in 3D space, if

$$\Psi(\underline{v}) = M. \tag{3}$$

This means that voxel v belongs to a seed cluster, if it projects on a seed projection in all of the images. We define $\mathbf{S}$ as a set that contains all the seed voxels.

After populating the VOI, the seed clusters are labeled using the connected component labeling algorithm.[53] We use these labeled clusters, their relation with the labeled images, and their centers and volumes in Sec. II D to find the seed centroids and remove the false positives.

Since we are only interested in voxels with a value of M, we can significantly increase the computational speed for VOI reconstruction using the following procedure.

At the beginning, all the voxels are initialized with a voxel value equal to zero. In the first iteration, all the voxels in the VOI are projected on the first image using Eq. (1). If a voxel projects on a seed projection in this image, its voxel value is increased by 1, otherwise its voxel value is kept unchanged (see Fig. 4). The voxels that have a value of zero after this iteration do not have the opportunity to acquire a value of M after projection on the subsequent $M-1$ images. Therefore, in the second iteration, only the voxels with a voxel value of 1 are projected on the second image and their voxel values are updated in the same manner. Likewise, in the ith iteration ($i \leq M$), only the voxels with a value of $(i-1)$ are projected. This decreases the number of projected voxels significantly after each iteration and increases the computational speed that is very important for clinical seed reconstruction. Since every voxel is projected on M images only, the maximum voxel value is equal to M. This forward-projection approach removes the risk of cross-talk between voxels that may occur in back-projection.

II.C. Motion compensation

The pose computation problem is equivalent to finding the transformation matrix ${}^{s}\mathbf{T}_{w}$ in Eq. (1). This matrix can be defined using the following equation:

$${}^{s}\mathbf{T}_{w} = \begin{bmatrix} {}^{s}\mathbf{R}_{w} & -{}^{s}\mathbf{R}_{w}\delta - \begin{bmatrix} 0 \\ 0 \\ l \end{bmatrix} \\ \mathbf{0}^{T} & 1 \end{bmatrix}, \tag{4}$$

where ${}^{s}\mathbf{R}_{w}$ is the rotation matrix from the world to the source coordinate frame, l is the distance from the source to the center of rotation, and $\delta = [\delta_x\ \delta_y\ \delta_z]^T$ is the translational motion of the C-arm caused by oscillation and sagging. We can initialize a pose estimation by measuring the C-arm rotation angles that define ${}^{s}\mathbf{R}_{w}$, and setting the unknown C-arm translational motion (δ) equal to zero. The error caused by assuming $\delta = 0$ can result in significant pose computation errors and consequently in unsuccessful reconstructions. Therefore, we should compensate for translational motions and improve on our pose computation.

As mentioned, Lee's autofocus method[37] is not applicable to our problem, due to the absence of the FTRAC. Therefore, we propose a different motion compensation schemes.

We observed that the cardinality of $\mathbf{S}$—the total number of seed voxels in the VOI—is maximized when the pose is accurately known. Figure 5 shows the cardinality of $\mathbf{S}$ as a function of C-arm translational pose errors in the up–down direction (along z_w) and perpendicular to the plane of rotation (along y_w). This figure shows a simulated case, in which the poses of 4 images are accurately known, and the errors

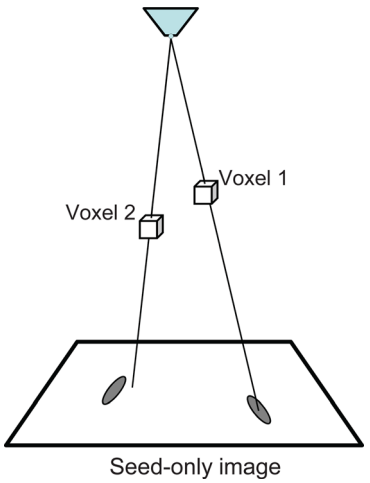

FIG. 4. Projection of two voxels on a seed-only image. In this projection, the voxel value of Voxel 1 is increased by one since Voxel 1 projects on a seed projection in this image. The voxel value of Voxel 2 is unchanged.

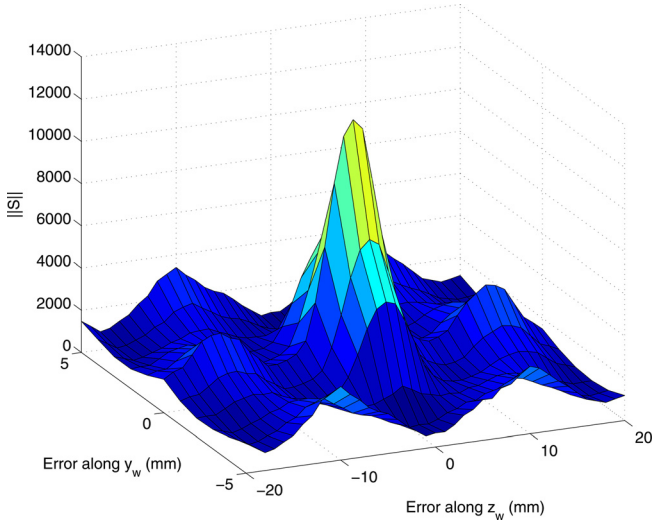

FIG. 5. The total number of seed voxels in a VOI as a function of pose estimation errors. Errors are in the up–down direction (along z_w) and perpendicular to the plane of rotation (along y_w).

are added to the 5th pose. Note that the cardinality of **S** is an integer-valued function.

In the motion compensation algorithm, we assume that the position of the C-arm corresponding to the first image (henceforth the first C-arm) is fixed in the 3D space and compensate for 2D motion of the rest of the C-arm positions by solving the following problem:

$$\begin{aligned} \delta_i^* &= \arg\max_{\delta_i} \|\mathbf{S}\|, \\ &\text{s.t.} \quad \delta_{xi} = 0, \\ &i \in \{2, \ldots, M\}, \end{aligned} \tag{5}$$

where $\|.\|$ denotes the cardinality of a set.

Note that unlike motion compensation methods introduced in the previous work,[25,37,48,49] this method does not require seeds to compensate for pose errors.

The optimization function in Eq. (5) is integer-valued. Furthermore, it has several local maximums, as can be seen in Fig. 5. In order to remedy these problems, we exploit the covariance matrix adaptation evolution strategy (CMA-ES).[54] This is a stochastic and gradient-free numerical optimization method suitable for nonlinear and nonconvex problems.

Although we benefit from a fast forward-projection method explained in Sec. II B, populating the VOI in every iteration can be time consuming depending on its size and resolution and the number of images. In order to reduce the computational time, the motion compensation is performed on a smaller VOI with a lower resolution. In addition, only a portion of each image is used to populate the smaller VOI.

Rotation of the C-arm around its PA results in horizontal motion of the seeds between images in a way that seed projections located at the top or bottom of one image appear at the top or bottom of the other images. Therefore, we use a narrow band from the top of each seed-only image to populate the smaller VOI during the motion compensation. The size of the VOI during motion compensation is adjusted according to the width of the band. We also observed that extra dilation of the band images increases the capture range of the optimization algorithm and also decreases the number of iterations required to obtain a sufficient motion compensation. Figure 6 shows a sample of a band image used for motion compensation. Note that this image is more dilated compared to the image in Fig. 3.

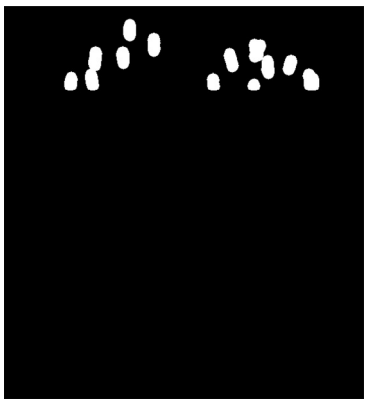

FIG. 6. A band image used for motion compensation.

II.D. Seed detection and false positive removal

After motion compensation, the VOI is populated using the improved pose computations. The seed voxels are labeled into different clusters using the so called connected component labeling algorithm.[53] Unfortunately, tomosynthesis-based seed reconstruction is prone to producing false positive (FP) seeds, due to the small number of images used (see Fig. 7). These false positive seeds should be removed before dose calculation to avoid overestimating the radiation dose.

The FPs are generated when M cone-shaped back projections from M seed projections intersect or touch in a voxel, which is not a true seed voxel. Therefore, the FP clusters usually have small volumes. However, due to errors in the pose computation (even after motion compensation) and calibration parameters, the clusters in the VOI have a wide range of volumes as shown by a histogram of the cluster volumes after motion compensation for a real patient in Fig. 8. Indeed, some of true seed clusters can have small volumes comparable to volume of a false positive cluster. Thus, an FP removal method purely based on the volume of clusters[34,36] can also remove some of the true seeds. Lee *et al.*[37] used an optimal coverage problem approach and a greedy search to remove the FP seeds. They found the minimum subset of the reconstructed seeds that covers all the seed projections in all the images. Looking at Fig. 7, one can see that if we remove any of the true seeds from the reconstructed seeds, we cannot cover all the seed projections in the seed-only images. Therefore, the three true seeds are the only subset of the reconstructed seeds that cover all the seed projections. However, it should be noted that due to seed projection overlap in the images, the smallest subset of the reconstructed seeds that cover all the projections has significantly fewer members than the number of implanted seeds. Therefore, we use information about the cluster volumes to add a necessary number of seeds to the covering subset to reconstruct all the implanted seeds.

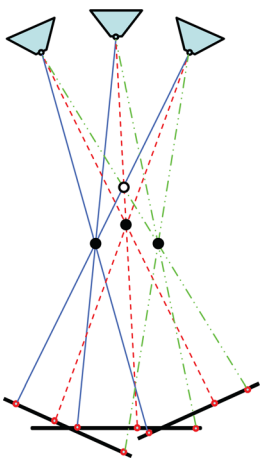

FIG. 7. A false positive seed (white circle) and three true seeds (black circles). If any of the true seeds are removed, one cannot cover all the seed projections in the images.

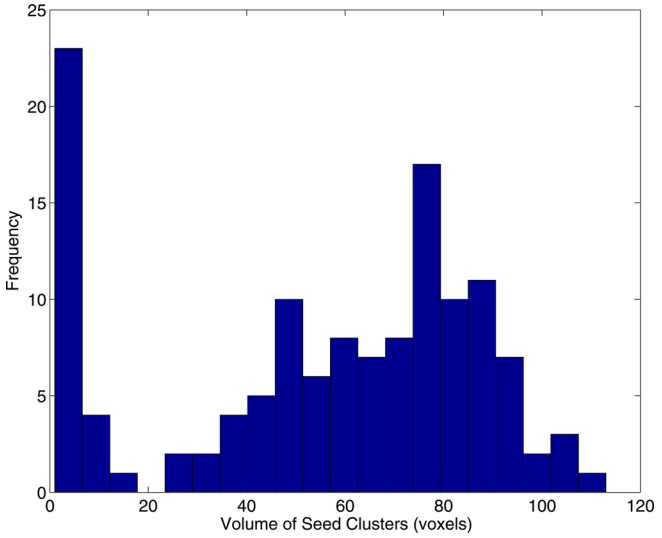

FIG. 8. Histogram of the seed cluster volumes for a real patient. Due to the wide range of cluster volumes, a predefined volume threshold cannot remove the FPs.

We take the following steps to identify and remove the false positives:

1. Clusters with large volumes are separated into multiple clusters. These clusters are generated when two seeds are located very close to each other. Although the seed positions are planned to be at least 5 mm away from each other, due to the seed misplacements, two seeds can be sufficiently close to each other to form a combined cluster. In this paper, we examine all clusters that have a volume greater than the median volume with a 6-neighbor connected component labeling (the initial labeling is performed using 26-neighbor connection). Usually, clusters that are barely touching can be separated into their constituent clusters. In addition, we divide the clusters that have a volume larger than αv_m ($\alpha = 2$ in this work), where v_m is the median volume.
2. The centroids of the seed clusters are calculated as seed candidates and reprojected on the labeled seed-only images.
3. At this point, we generate a $N_t \times M$ assignment table, where N_t is the total number of reconstructed seed centroids (N is the number of implanted seeds). Entry (i,j) of the assignment table shows the label of the seed projection in image j where the ith seed centroid is projected.
4. If two or more seed centroids project on similar seed projections in all the images (have identical rows in the assignment table), the one with the largest cluster volume is saved and the rest are removed, unless the seeds are from a separated large cluster. The seeds that are separated from a large cluster in step 1 are marked and will not be removed.
5. The seed centroids that project on at least one unique seed projection in one image are marked as unique seed centroids and are preserved regardless of their cluster volume. If we remove any of these seeds, we cannot cover all the seed projections.
6. Seed centroids that have a cluster volume smaller than a threshold (20% of the median volume in this work) and are not one of the unique seeds are removed.
7. The list of unique seeds is updated after removal of small clusters. Assume N_u unique seeds are available at this stage. The rest of the seeds share all of their seed projections with other seed centroids. Due to the seed projection overlap (see Figs. 1 or 3), the number of unique seeds is less than the number of implanted seeds.
8. Finally, we add $N - N_u$ seeds with maximum cluster volumes from the remaining seeds to the unique seeds to reconstruct N seeds in total.

II.E. Numerical simulations

Four seed clouds were simulated based on four realistic implant plans with 100, 108, 110, and 130 seeds. Seeds were simulated as capsules with diameter of 1 mm and length of 4.5 mm, approximately equal to the radio-opaque size of ^{125}I seeds. The relative positions of the seed centroids were imported from the plan. We assumed that the long axis of the capsules is parallel to the y_w axis. Seed-only images were synthesized by rotating the C-arm around its PA by angles of $0°, \pm 5°$, and $\pm 10°$, while the SA angle was kept constantly at 180°. Translational errors of 0–5 mm along the y_w axis with steps of 1 mm and 0–20 mm along the z_w with steps of 2 mm were independently applied to one of the C-arm poses. All of the five images were used to reconstruct the seeds, with and without motion compensation. Intrinsic parameters of a GE OEC® 9800 mobile C-arm were used in the simulations.

II.F. Phantom validation

A CIRS Model-053 prostate brachytherapy training phantom (CIRS Inc., Norfolk, VA) was used in our phantom study. An experienced brachytherapist implanted 136 dummy stranded seeds using 26 needles, based on a realistic implant plan prepared by a board-certified medical physicist. A motorized GE OEC 9800 mobile C-arm was used to acquire five images by rotating the device around its PA in a 20° rotation span in approximately 5° intervals. Rotation angles were measured using a digital protractor attached to the C-arm source casing. In order to establish a ground truth, the phantom was also scanned with a Picker PQ5000 CT scanner. We segmented the seeds in the CT volume by thresholding.

II.G. Patient study

Ten patients were implanted with 100–135 (average 112) stranded ^{125}I seeds at the British Columbia Cancer Agency (Vancouver, BC, Canada). The patients had a prescribed dose of 144.0 Gy and an average prostate target volume (PTV) of 54.5 cc. For each patient, five images were taken using a motorized GE OEC 9800. This device has a heavy intensifier that causes significant sagging and necessitates motion compensation for seed reconstruction. The C-arm was rotated around its PA, which was aligned with the craniocaudal axis of the patient. The images were taken at angles of

approximately $0°, \pm 5°$, and $\pm 10°$. Rotation angles were measured using a digital protractor or the device joint encoders. The digital protractor had a resolution of 0.1° and the joint encoders had a resolution of 1°. The rotation angle around SA was fixed at 180°. However, deviations of 1° were observed according to the C-arm joint encoders. These deviations were taken into account during the seed reconstruction.

The C-arm was calibrated preoperatively. We assumed that the C-arm intrinsic parameters were constant for all the rotation angles and patients. The seeds were reconstructed in a $65 \times 80 \times 70$ mm^3 VOI with a voxel size of $0.25 \times 0.5 \times 0.5$ mm^3 and image dilation radius of 2 or 3 pixels. During the motion compensation, band images with band width of 150 pixels and dilation radius of 6 pixels were used for all the patients. A $65 \times 10 \times 70$ mm^3 VOI with a voxel size of $1 \times 1 \times 1$ mm^3 was used to achieve higher speeds.

III. RESULTS

III.A. Numerical simulations

For numerical simulations, the localization error was measured as the distance between the reconstructed and synthesized seeds after a rigid registration. Figure 9 shows the seed detection rate and localization error of the reconstructed seeds versus the introduced pose error. As it can be seen, motion-compensated seed reconstruction is able to maintain high seed detection rates and low localization errors, despite the presence of translational pose errors, while the reconstruction without motion compensation fails.

III.B. Phantom study

The seeds reconstructed using the motion-compensated tomosynthesis were compared with the seeds segmented in CT after a rigid registration. Although the CT and fluoroscopy images were taken at different times, we assumed that the phantom deformation and seed displacements were negligible. We achieved a 100% seed detection rate with 0.86 ± 0.44 mm (Mean $\pm$ STD) localization difference between CT and C-arm-based reconstructions.

III.C. Clinical results

For our clinical data sets, we reprojected the reconstructed seeds on the C-arm images as shown in Fig. 10. As it can be seen, hidden and overlapping seeds were successfully reconstructed. The images were meticulously inspected for missing seeds. The seed detection rate for each patient is reported in Table I.

Since the real positions of the seeds were unknown, we compared our results with the results of an available motion-compensated matching-based seed reconstruction method[49] after a rigid registration and reported the registration error in Table I.

We achieved an average seed detection rate of 99.5%, which is a clinically excellent result. Su *et al.*[55] showed that in ^{125}I prostate implants a seed detection rate of above 95% is sufficient to achieve clinically accurate dose calculations. Our seed detection rates are above this threshold for all the patients. The seed detection rate without motion compensation

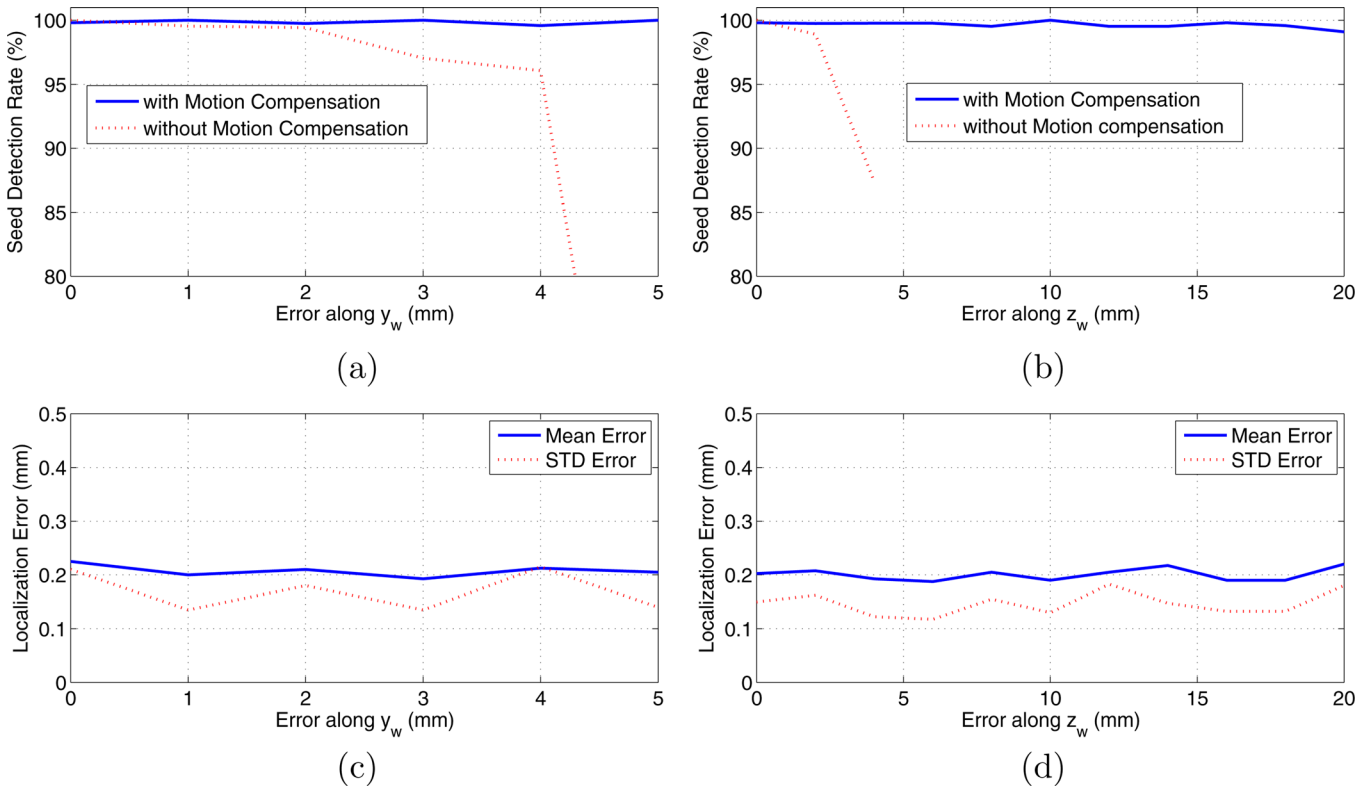

FIG. 9. Simulation results, showing the average seed detection rate and localization error for variable pose errors. The average of seed detection rate for errors along y_w and z_w are shown in (a) and (b), respectively, for reconstructions with and without motion compensation. The mean and STD of localization error for errors along y_w and z_w are shown in (c) and (d), respectively, for reconstruction with motion compensation.

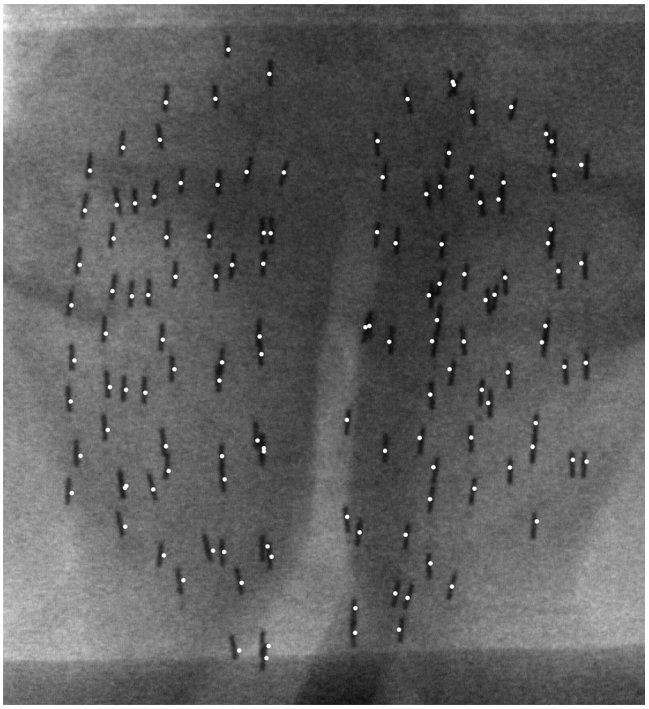

FIG. 10. Reconstructed seed centroids projected on the C-arm image.

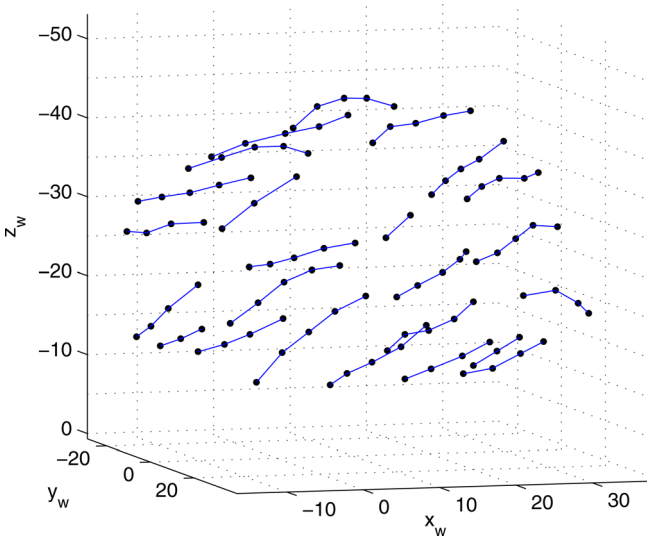

FIG. 11. Reconstructed seed centroids. Seeds on the same strand are connected to each other.

was on average below 50%. This shows the necessity of motion compensation, when only C-arm rotation angles are measured.

We used five images for eight of the patients. For patients 9 and 10, seed detection using four images was more successful. This was due to inaccurate rotation angle measurement for one of the images, most likely caused by inaccurate reading of the encoder or protractor while the C-arm was still oscillating. Grzeda and Fichtinger[50] used accelerometers to measure the C-arm rotation angles with high accuracy. In addition, the accelerometer can sense the C-arm oscillation and send a signal to the operator when the oscillation is sufficiently decayed. Therefore, using accelerometers results in more accurate rotation angle measurement and sharper images.

In the case of the stranded ^{125}I seeds used in our clinical study, the seeds in a strand are kept at a fixed center-to-center distance of 10 mm. In order to gain more confidence in the reconstruction results and confirm that no significant scaling occurred, we calculated the center-to-center distance of the reconstructed seeds in the different strands.[56] Figure 11 shows a reconstruction, in which seeds are grouped based on their strand. Table II shows the mean and STD of interseed spacing for all the patients. The interseed spacing has an overall average of 10.3 mm, demonstrating an insignificant scaling effect.

IV. DISCUSSION

IV.A. Large cluster separation

In a brachytherapy plan, seeds are located at least 5 mm apart from each other. Due to a seed misplacement or migration, two seeds may be located sufficiently close to each other to create a combined seed cluster in the VOI. In the case of stranded seeds, two consecutive seeds cannot move toward each other to create a combined cluster. Nevertheless, two adjacent seeds that are not on the same strand may be located sufficiently close to each other to create a combined cluster.

TABLE I. The clinical results. The reconstruction rate is assessed visually based on the projection of the reconstructed seeds on the images. The difference reports the registration error between seed locations computed using the proposed method and an available seed reconstruction method.

Patient #	Number of seeds	Detection rate (%)	Difference (mm) mean ± STD	Dilation radius (pixel)
1	105	100.0	0.4 ± 0.3	2
2	105	100.0	0.3 ± 0.4	2
3	135	100.0	0.4 ± 0.3	3
4	102	99.0	0.4 ± 0.3	2
5	122	100.0	0.6 ± 0.4	2
6	113	100.0	0.5 ± 0.3	2
7	100	98.0	0.5 ± 0.5	2
8	120	99.2	0.9 ± 0.5	3
9[a]	104	98.1	0.5 ± 0.3	2
10[a]	115	99.2	0.6 ± 0.4	2

[a]For patients 9 and 10, only four images were used.

TABLE II. The mean and STD of the distance between two consecutive seeds on a strand.

Patient #	Seed spacing (mm) mean ± STD
1	10.3 ± 0.4
2	10.3 ± 0.3
3	10.3 ± 0.3
4	10.3 ± 0.3
5	10.3 ± 0.5
6	10.2 ± 0.4
7	10.4 ± 0.6
8	10.0 ± 0.5
9	10.4 ± 0.3
10	10.2 ± 0.4
Overall	10.3 ± 0.4

Due to C-arm calibration and pose computation errors (even after motion compensation), the seed clusters have a wide range of volumes (see Fig. 8). In addition, if two seeds are very close to each other, the volume of the merged cluster will not be significantly larger than a single-seed cluster. Therefore, detection of multiple-seed clusters is not possible by using a uniform threshold on the volume.

As mentioned, ^{125}I seeds have larger seed projections compared to ^{103}Pd seeds, which lead to more overlapping seed projections in the images, which in turn increase the likelihood of having combined clusters in the VOI. In addition, the seed density can affect the likelihood of formation of combined clusters. Our patients had a seed density of approximately 2 seeds per milliliter (total number of seeds divided by PTV), with more concentration at the posterior-peripheral region.[3] In treatment plans with a lower seed density, the seeds are more separated and merged clusters are less likely to form.

IV.B. Determination of seed dilation radius

Even after motion compensation, the reconstruction may suffer from minor errors in the rotation angle measurement, calibration parameters, and geometric distortion as well as from motion along the x_w axis. Since seed clusters are formed at the intersection of rays that emanate from a seed projection toward the x-ray source, seed-only image dilation can decrease the effects of the aforementioned errors as it can increase the likelihood of seed detection by increasing the size of the seed projections. However, if the dilation radius is too large, the seed clusters will grow in size and ultimately merge. Therefore, the best dilation radius should be chosen specifically based on the pose and parameter estimation errors. We used a dilation radius of 2 pixels in the numerical simulations and phantom study and a radius of 2 or 3 pixels for the patient data sets (see Table I). However, it should be noted that a fixed dilation radius of 6 pixels was used during the motion compensation phase in simulation, phantom, and clinical studies. Since motion compensation is the most time consuming part of the seed reconstruction algorithm, it is possible to use a fixed dilation radius for motion compensation, then adjust the dilation radius during final VOI reconstruction and seed detection. The final VOI reconstruction and seed detection take approximately 5 s of runtime.

A variable dilation radius can be helpful in increasing the detection rate without increasing the large clusters. In such a method, the dilation radius will be larger for images or part of images that are affected more by the aforementioned errors, while a small dilation radius can be applied where the errors are small. Investigation on variable dilation radius is part of the future work.

IV.C. Localization error

In contemporary brachytherapy, implants are assessed using CT, one or several days after the procedure. C-arm images are, however, taken during or at the end of the procedure, while the patient is still in treatment position. In addition, in our case, the TRUS probe was still partially inside the rectum during C-arm imaging, while the CT scan was performed without the TRUS. Due to prostate swelling during and after brachytherapy,[7] postimplant seed migration,[8] and probe pressure, seed positions during CT scan were different from the position of the seeds when the C-arm images were taken. Therefore, CT images of the patient could not be used to establish a confident ground truth for the position of the seeds in 3D. For this reason, we relied on the projection of the reconstructed seeds on the images and on the comparison with the results of another reconstruction method to assess our reconstructions.

It was shown that a localization uncertainty of less than 2 mm results in less than 5% deviation in the prostate D90 (the minimum dose delivered to 90% of the prostate).[57,58] Although we could not measure the seed localization error for our clinical data sets, the localization errors in our numerical simulations and phantom studies were significantly lower than this threshold.

IV.D. Computation time

We implemented our algorithm using MATLAB on a PC with an Intel 2.33 GHz Core2 Quad CPU and 3.25 GB of RAM. MATLAB implementation of CMA-ES algorithm was provided by N. Hansen.[59] The CMA-ES algorithm shows faster convergence if the parameter search region is limited. Thus, we limited the search region to ± 30 mm along the z_w axis and ± 3 mm along y_w. We used the center of mass of the seed-only images to initialize the displacement along y_w. Therefore, displacements of larger than 3 mm in this direction could be recovered in the simulation studies. This search region was sufficiently large for all clinical data sets.

The criterion to terminate the optimization was set to 2000 function evaluations. This resulted in a constant reconstruction time of approximately 1 min per patient (excluding the production of seed-only images). Our code was not optimized for computational speed. We expect to gain faster performance using an optimized C++ implementation. Band images and a smaller VOI with lower resolution were used during the motion compensation phase to decrease the

computation time. Investigation on the optimal image band width and the size and resolution of the VOI for the least computational cost are part of our future work.

On our patient data sets, we achieved an average seed detection rate of 99.5% with computational time of approximately 1 min per patient. Similar detection rates were reported using previously published tomosynthesis-based reconstruction methods. In particular, Lee *et al.*[37] reported an average detection rate of 98.8% in approximately 100 s per patient and Brunet-Benkhoucha *et al.*[36] reported an average detection rate of 96.7% with 36.5 s average computational time. Brunet-Benkhoucha *et al.* used a radiotherapy simulator, which is a precisely calibrated and accurately tracked device. Hence, they did not require motion compensation.[36] As discussed before, Lee *et al.*[37] used the FTRAC (Ref. 46) to initialize a pose estimation and also choose the best images to reconstruct some seeds for seed-based motion compensation. The same radio-opaque fiducial was also used by Jain *et al.*,[30] Kon *et al.*,[31] and Lee *et al.*[32] to reconstruct the seeds using a matching-based approach. In these works, the pose computation accuracy provided by the FTRAC was sufficient for high detection rates without motion compensation. As mentioned, employing such a fiducial requires an additional segmentation task. Furthermore, image acquisition in presence of this fiducial is more complicated in order to avoid an overlap between the fiducial image and the seed projections.

In our previous work,[49] we achieved an average seed reconstruction rate of 98.5% with average computational time of 19.8 s per patient using three images in a motion-compensated matching-based reconstruction. Although the detection rate in the current paper is only slightly better than our previous work, the true advantage of the current work is in enabling motion compensation with tomosynthesis-based reconstruction. As discussed earlier, matching-based seed reconstruction methods require a more complicated seed segmentation algorithm as they require the seed projection centroids, which are difficult to localize in the presence of hidden and overlapping projections. Especially for ^{125}I seeds that have relatively longer seed projections, overlapping seeds are more common in the projection images. For this reason, in our previous work, we relied on manual seed segmentation which is a time consuming task. Compared to matching-based reconstructions, tomosynthesis-based reconstruction methods require a simple image processing step to separate the seed projection regions from the background. Therefore, our current work introduces an alternative solution for seed reconstruction, which is especially attractive for reconstruction of ^{125}I seeds. We should emphasize that the motion compensation method proposed in our previous work is not applicable to tomosynthesis.

As mentioned in Sec. II C, rotation of the C-arm around its PA results in horizontal movement of the seed projections between images. If the C-arm rotates around its SA, the seed projections move along vertical lines in the images. Therefore, vertical bands from the sides of the images can be used for motion compensation. Similarly to our case, the motion in the up–down direction and perpendicular to the plane of rotation should be compensated.

We used the constant center-to-center distance of the stranded seeds to show that no significant scaling occurred. However, the motion compensation and reconstruction methods do not rely on any information limited to stranded seeds. Therefore, we expect similar performance for non-stranded seeds.

The motion compensation method can be extended to use more images at the expense of computational time. Increasing the number of images can reduce the number of false positives and increase the seed detection rate. It can also decrease the likelihood of formation of merged clusters by decreasing the volume of seed clusters. The same effect can be achieved by using a wider rotation span.

In our case, we assumed that the image geometric distortion was negligible as we positioned the C-arm to capture the seed projections close to the center of the image. However, correction of the geometric image distortion can increase the seed detection rate and improve the localization accuracy. Although image distortion is pose dependent, Jain *et al.*[51] showed that in small rotation spans, the correction parameters obtained from an image acquired in the center of the rotation span can considerably correct for the distortion of all the images with insignificant relative deviation in reconstructed seed positions.

V. CONCLUSIONS AND FUTURE WORK

We introduced a computational 2D motion compensation algorithm for tomosynthesis-based seed reconstruction from C-arm images. We initialized the C-arm pose using sole measurements of rotation angles, and we compensated for C-arm motions in the up–down direction and perpendicular to the plane of rotation by maximizing the number of seed voxels in the volume of interest. Our method does not require reconstructed seeds for motion compensation. Therefore, it can be used to recover from severe pose errors that inhibit reconstruction of a sufficient number of initial seeds.

In a clinical study on ten patients, we measured the C-arm rotation angle around its PA using a digital protractor and C-arm joint encoders. Seed reconstruction with motion compensation achieved an average seed detection rate of 99.5%, which is a clinically excellent result, with a 1 min per patient reconstruction time. We also achieved 100% seed detection rate with 0.86 ± 0.44 mm localization error in a phantom study.

Our motion compensation algorithm obviates the need for full pose tracking with radio-opaque fiducials or other external trackers. Considering the simplicity of implementation and high seed detection rates, our algorithm appears to be feasible for clinical application.

Two dimensional motion of the C-arm was an essential assumption in this work. Extension of our motion compensation to 3D and removing the scaling effect using the inter-seed spacing are part of the future work.

ACKNOWLEDGMENTS

The authors would like to thank Lauren Gordon, B.Sc. for preparing the code for seed grouping. Ehsan Dehghan was

supported by an Ontario Ministry of Research and Innovation postdoctoral fellowship. Mehdi Moradi was supported by Natural Sciences and Engineering Research Council of Canada, and US Army Medical Research and Material Command under W81XWH-10-1-0201. W. James Morris is the principal investigator on two randomized control trials that are sponsored, in part, by unrestricted educational grants from Oncura corporation, which makes the ^{125}I sources used in the study. Gabor Fichtinger was supported as Cancer Care Ontario Research Chair. This work was supported in part by NIH Grant No. R21CA120232-01.

[a]Author to whom correspondence should be addressed. Electronic mail: tims@ece.ubc.ca

[1]A. Jemal, R. Siegel, J. Xu, and E. Ward, "Cancer statistics, 2010," Ca-A Cancer J. Clin. **60**, 277–300 (2010).

[2]J. C. Blasko, T. Mate, J. E. Sylvester, P. D. Grimm, and W. Cavanagh, "Brachytherapy for carcinoma of the prostate: Techniques, patient selection, and clinical outcomes," Semin. Radiat. Oncol. **12**, 81–94 (2002).

[3]W. Morris, M. Keyes, D. Palma, I. Spadinger, M. McKenzie, A. Agranovich, T. Pickles, M. Liu, W. Kwan, J. Wu, E. Berthelet, and H. Pai, "Population-based study of biochemical and survival outcomes after permanent ^{125}I brachytherapy for low- and intermediate-risk prostate cancer," Urology **73**, 860–865 (2009).

[4]W. J. Morris, M. Keyes, D. Palma, M. McKenzie, I. Spadinger, A. Agranovich, T. Pickles, M. Liu, W. Kwan, J. Wu, V. Lapointe, E. Berthelet, H. Pai, R. Harrison, W. Kwa, J. Bucci, V. Racz, and R. Woods, "Evaluation of dosimetric parameters and disease response after ^{125}iodine transperineal brachytherapy for low- and intermediate-risk prostate cancer," Int. J. Radiat. Oncol., Biol., Phys. **73**, 1432–1438 (2009).

[5]B. R. Prestidge, J. J. Prete, T. A. Buchholz, J. L. Friedland, R. G. Stock, P. D. Grimm, and W. S. Bice, "A survey of current clinical practice of permanent prostate brachytherapy in the United States," Int. J. Radiat. Oncol., Biol., Phys. **40**, 461–465 (1998).

[6]V. Lagerburg, M. A. Moerland, J. J. Lagendijk, and J. J. Battermann, "Measurement of prostate rotation during insertion of needles for brachytherapy," Radiother. Oncol. **77**, 318–323 (2005).

[7]Y. Yamada, L. Potters, M. Zaider, G. Cohen, E. Venkatraman, and M. J. Zelefsky, "Impact of intraoperative edema during transperineal permanent prostate brachytherapy on computer-optimized and preimplant planning techniques," Am. J. Clin. Oncol. **26**, e130–e135 (2003).

[8]D. B. Fuller, J. A. Koziol, and A. C. Feng, "Prostate brachytherapy seed migration and dosimetry: Analysis of stranded sources and other potential predictive factors," Brachytherapy **3**, 10–19 (2004).

[9]S. Nag, J. P. Ciezki, R. Cormak, S. Doggett, K. Dewyngaert, G. K. Edmundson, R. G. Stock, N. N. Stone, Y. Yan, and M. J. Zelefsky, "Intraoperative planning and evaluation of permanent prostate brachytherapy: Report of the American brachytherapy society," Int. J. Radiat. Oncol., Biol., Phys. **51**, 1422–1430 (2001).

[10]P. F. Orio III, I. B. Tutar, S. Narayanan, S. Arthurs, P. S. Cho, Y. Kim, G. Merrick, and K. E. Wallner, "Intraoperative ultrasound-fluoroscopy fusion can enhance prostate brachytherapy quality," Int. J. Radiat. Oncol., Biol., Phys. **69**, 302–307 (2007).

[11]A. Polo, C. Salembier, J. Venselaar, and P. Hoskin, "Review of intraoperative imaging and planning techniques in permanent seed prostate brachytherapy," Radiother. Oncol. **94**, 12–23 (2010).

[12]B. H. Han, K. Wallner, G. Merrick, W. Butler, S. Sutlief, and J. Sylvester, "Prostate brachytherapy seed identification on post-implant TRUS images," Med. Phys. **30**, 898–900 (2003).

[13]E. J. Feleppa, S. Ramachandran, S. K. Alam, A. Kalisz, J. A. Ketterling, R. D. Ennis, and C.-S. Wuu, "Novel methods of analyzing radiofrequency echo signals for the purpose of imaging brachytherapy seeds used to treat prostate cancer," Proc SPIE, **4687**, 127–138 (2002).

[14]S. McAleavey, D. Rubens, and K. Parker, "Doppler ultrasound imaging of magnetically vibrated brachytherapy seeds," IEEE Trans. Biomed. Eng. **50**, 252–254 (2003).

[15]F. Mitri, P. Trompette, and J.-Y. Chapelon, "Improving the use of vibroacoustography for brachytherapy metal seed imaging: A feasibility study," IEEE Trans. Med. Imaging **23**, 1–6 (2004).

[16]M. Ding, Z. Wei, L. Gardi, D. B. Downey, and A. Fenster, "Needle and seed segmentation in intra-operative 3D ultrasound-guided prostate brachytherapy," Ultrasonics **44**, e331–e336 (2006), Proceedings of Ultrasonics International (UI'05) and World Congress on Ultrasonics (WCU).

[17]Z. Wei, L. Gardi, D. B. Downey, and A. Fenster, "Automated localization of implanted seeds in 3D TRUS images used for prostate brachytherapy," Med. Phys. **33**, 2404–2417 (2006).

[18]X. Wen, S. E. Salcudean, and P. D. Lawrence, "Detection of brachytherapy seeds using 3D transrectal ultrasound," IEEE Trans. Biomed. Eng. **57**, 2467–2477 (2010).

[19]D. F. French, J. Morris, M. Keyes, O. Goksel, and S. E. Salcudean, "Intraoperative dosimetry for prostate brachytherapy from fused ultrasound and fluoroscopy images," Acad. Radiol. **12**, 1262–1272 (2005).

[20]Y. Su, B. J. Davis, M. G. Herman, and R. A. Robb, "TRUS-fluoroscopy fusion for intraoperative prostate brachytherapy dosimetry," Studies in Health Technology and Informatics, **119**, 532–537 (2006).

[21]I. B. Tutar, L. Gong, S. Narayanan, S. D. Pathak, P. S. Cho, K. Wallner, and Y. Kim, "Seed-based transrectal ultrasound-fluoroscopy registration method for intraoperative dosimetry analysis of prostate brachytherapy," Med. Phys. **35**, 840–848 (2008).

[22]P. Fallavollita, Z. Karim-Aghaloo, E. Burdette, D. Song, P. Abolmaesumi, and G. Fichtinger, "Registration between ultrasound and fluoroscopy or CT in prostate brachytherapy," Med. Phys. **37**, 2749–2760 (2010).

[23]H. I. Amols and I. I. Rosen, "A three-film technique for reconstruction of radioactive seed implants," Med. Phys. **8**, 210–214 (1981).

[24]T. M. Persons, R. L. Webber, P. F. Hemler, W. Bettermann, and J. D. Bourland, "Brachytherapy volume visualization," Proc. SPIE, **3976**, 45–56 (2000).

[25]D. Tubic, A. Zaccarin, L. Beaulieu, and J. Pouliot, "Automated seed detection and three-dimensional reconstruction. II. Reconstruction of permanent prostate implants using simulated annealing," Med. Phys. **28**, 2272–2279 (2001).

[26]D. A. Todor, G. N. Cohen, H. I. Amols, and M. Zaider, "Operator-free, film-based 3D seed reconstruction in brachytherapy," Phys. Med. Biol. **47**, 2031–2048 (2002).

[27]Y. Su, B. J. Davis, M. G. Herman, and R. A. Robb, "Prostate brachytherapy seed localization by analysis of multiple projections: Identifying and addressing the seed overlap problem," Med. Phys. **31**, 1277–1287 (2004).

[28]S. Narayanan, P. S. Cho, and R. J. Marks II, "Three-dimensional seed reconstruction from an incomplete data set for prostate brachytherapy," Phys. Med. Biol. **49**, 3483–3494 (2004).

[29]S. T. Lam, P. S. Cho, R. J. Marks II, and S. Narayanan, "Three-dimensional seed reconstruction for prostate brachytherapy using Hough trajectories," Phys. Med. Biol. **49**, 557–569 (2004).

[30]A. K. Jain, Y. Zhou, T. Mustufa, E. C. Burdette, G. S. Chirikjian, and G. Fichtinger, "Matching and reconstruction of brachytherapy seeds using the Hungarian algorithm (MARSHAL)," Med. Phys. **32**, 3475–3492 (2005).

[31]R. C. Kon, A. K. Jain, and G. Fichtinger, "Hidden seed reconstruction from C-arm images in brachytherapy," *IEEE International Symposium on Biomedical Imaging: Nano to Macro* (Arlington, Virginia, 2006).

[32]J. Lee, C. Labat, A. K. Jain, D. Y. Song, E. C. Burdette, G. Fichtinger, and J. L. Prince, "REDMAPS: Reduced-dimensionality matching for prostate brachytherapy seed reconstruction," IEEE Trans. Med. Imaging **30**, 38–51 (2011).

[33]G. Messaris, Z. Kolitsi, C. Badea, and N. Pallikarakis, "Three-dimensional localisation based on projectional and tomographic image correlation: an application for digital tomosynthesis," Med. Eng. Phys. **21**, 101–109 (1999).

[34]I. B. Tutar, R. Managuli, V. Shamdasani, P. S. Cho, S. D. Pathak, and Y. Kim, "Tomosynthesis-based localization of radioactive seeds in prostate brachytherapy," Med. Phys. **30**, 3135–3142 (2003).

[35]X. Liu, A. K. Jain, and G. Fichtinger, "Prostate implant reconstruction with discrete tomography," MICCAI 2007, Lecture Notes in Computer Science 4791, Springer Berlin/Heidelberg, pp. 734–742.

[36]M. Brunet-Benkhoucha, F. Verhaegen, B. Reniers, S. Lassalle, D. Béliveau-Nadeau, D. Donath, D. Taussky, and J.-F. Carrier, "Clinical implementation of a digital tomosynthesis-based seed reconstruction algorithm for intraoperative postimplant dose evaluation in low dose rate prostate brachytherapy," Med. Phys. **36**, 5235–5244 (2009).

[37]J. Lee, X. Liu, A. Jain, D. Song, E. Burdette, J. Prince, and G. Fichtinger, "Prostate brachytherapy seed reconstruction with Gaussian blurring and optimal coverage cost," IEEE Trans. Med. Imaging **28**, 1955–1968 (2009).

[38]D. Pokhrel, M. J. Murphy, D. A. Todor, E. Weiss, and J. F. Williamson, "Reconstruction of brachytherapy seed positions and orientations from cone-beam CT x-ray projections via a novel iterative forward projection matching method," Med. Phys. **38**, 474–486 (2011).
[39]S. T. Lam, R. J. Marks II, and P. S. Cho, "Prostate brachytherapy seed segmentation using spoke transform," Proc. SPIE, **4322**, 1490–1500 (2001).
[40]D. Tubic, A. Zaccarin, J. Pouliot, and L. Beaulieu, "Automated seed detection and three-dimensional reconstruction. I. seed localization from fluoroscopic images or radiographs," Med. Phys. **28**, 2265–2271 (2001).
[41]N. Kuo, J. Lee, A. Deguet, D. Song, E. C. Burdette, and J. Prince, "Automatic segmentation of seeds and fluoroscope tracking (FTRAC) fiducial in prostate brachytherapy x-ray images," Proc. SPIE, **7625**, 76252T1 (2010).
[42]T. Peters and K. Cleary, eds., *Image-Guided Interventions: Technology and Applications* (Springer Science+Business Media, New York, 2008).
[43]N. Navab, A. Bani-Hashemi, M. Mitschke, D. W. Holdsworth, R. Fahrig, A. J. Fox, and R. Graumann, "Dynamic geometrical calibration for 3D cerebral angiography," Proc. SPIE **2708**, 361–370 (1996).
[44]C. Brack, H. Götte, F. Gossé, J. Moctezuma, M. Roth, and A. Schweikard, "Towards accurate X-ray camera calibration in computer-assisted robotic surgery," *Proceedings of the International Symposium on Computer Assisted Radiology* (Paris, France, 1996), pp. 721–728.
[45]M. Zhang, M. Zaider, M. Worman, and G. Cohen, "On the question of 3D seed reconstruction in prostate brachytherapy: The determination of x-ray source and film locations," Phys. Med. Biol. **49**, N335–N345 (2004).
[46]A. K. Jain, T. Mustufa, Y. Zhou, C. Burdette, G. S. Chirikjian, and G. Fichtinger, "FTRAC—A robust fluoroscope tracking fiducial," Med. Phys. **32**, 3185–3198 (2005).
[47]P. Fallavollita, E. C. Burdette, D. Y. Song, P. Abolmaesumi and G. Fichtinger, "Technical Note: Unsupervised C-arm pose tracking with radiographic fiducial," Med. Phys. **38**, 2241–2245 (2011).
[48]A. Jain and G. Fichtinger, "C-arm tracking and reconstruction without an external tracker," MICCAI 2006, Lecture Notes on Computer Science 4190, Springer Berlin/Heidelberg, pp. 494–502.
[49]E. Dehghan, A. K. Jain, M. Moradi, X. Wen, W. J. Morris, S. E. Salcudean, and G. Fichtinger, "Brachytherapy seed reconstruction with joint-encoded C-arm single-axis rotation and motion compensation," Med. Image Anal. **15**, 760–771 (2011).
[50]V. Grzeda and G. Fichtinger, "Rotational encoding of C-arm fluoroscope with tilt sensing accelerometer," MICCAI 2010, Lecture Notes in Computer Science 6363, Springer Berlin/Heidelberg, pp. 424–431.
[51]A. Jain, M. An, N. Chitphakdithai, G. Chintalapani, and G. Fichtinger, "C-arm calibration—Is it really necessary?," *Proceedings of SPIE*, edited by K. Cleary and M. I. Miga (2007), Vol. 6509, 65092U-1–65092U-16.
[52]D. G. French, "Real-time dosimetry for prostate brachytherapy using TRUS and fluoroscopy," Master's thesis, University of British Columbia, Vancouver, BC, Canada, December 2004.
[53]R. M. Haralick and L. G. Shapiro, *Computer and Robot Vision*, (Addison-Wesley, Boston, 1992), Vol. 1, pp. 28–48.
[54]N. Hansen, "The CMA evolution strategy: A comparing review," *Towards a New Evolutionary Computation. Advances on Estimation of Distribution Algorithms*, Studies in Fuzziness and Soft Computing, edited by J. A. Lozano, P. Larranaga, I. Inza, and E. Bengoetxea (Springer, Berlin/Heidelberg, 2006), Vol. 192, pp. 75–102.
[55]Y. Su, B. J. Davis, M. G. Herman, A. Manduca, and R. A. Robb, "Examination of dosimetry accuracy as a function of seed detection rate in permanent prostate brachytherapy," Med. Phys. **32**, 3049–3056 (2005).
[56]L. Gordon, E. Dehghan, S. E. Salcudean, and G. Fichtinger, "Reconstruction of needle tracts from fluoroscopy images in prostate brachytherapy," *Proceedings of the 22nd International Conference of the Society for Medical Innovation and Technology (SMIT)* (Trondheim, Norway, 2010).
[57]P. E. Lindsay, J. Van Dyk, and J. J. Battista, "A systematic study of imaging uncertainties and their impact on ^{125}I prostate brachytherapy dose evaluation," Med. Phys. **30**, 1897–1908 (2003).
[58]Y. Su, B. J. Davis, K. M. Furutani, M. G. Herman, and R. A. Robb, "Dosimetry accuracy as a function of seed localization uncertainty in permanent prostate brachytherapy: Increased seed number correlates with less variability in prostate dosimetry," Phys. Med. Biol. **52**, 3105–3119 (2007).
[59]Available online at: http://www.lri.fr/ hansen/cmaes_inmatlab.html.